ACS APPLIED MATERIALS & INTERFACES

Research Article

www.acsami.org

Polyol-Mediated Synthesis of Mesoporous α-Ni(OH)$_2$ with Enhanced Supercapacitance

Hongmei Du, Lifang Jiao,* Kangzhe Cao, Yijing Wang, and Huatang Yuan

Institute of New Energy Material Chemistry, Key Laboratory of Advanced Energy Materials Chemistry(MOE), Tianjin Key Lab of Metal and Molecule-based Material Chemistry, Nankai University, Tianjin 300071, P.R. China

ABSTRACT: Flower-like α-Ni(OH)$_2$ microspheres composed of nanowires are prepared by a solvothermal method using triethylene glycol and water as the mixed solvent. The formation of this unique structure is attributed to the synergetic effect of dissolution-recrystallization procedure, Ostwald ripening, and aggregative lateral attachment. Experimental results indicate that the dielectric constant, viscosity, and the chain lengths of the alcohols in the solvent may greatly affect the morphology and size of the as-obtained α-Ni(OH)$_2$ samples. Because of the high Brunauer, Emmett, and Teller (BET) nitrogen sorption surface area of 318 m^2 g^{-1} and large pore volume, this sample displays a maximum discharge specific capacity of 1788.9 F g^{-1} at a discharge current density of 0.5 A g^{-1}. Besides, rate performance of this sample is also excellent, indicating that this sample is promising in electrochemical supercapacitors.

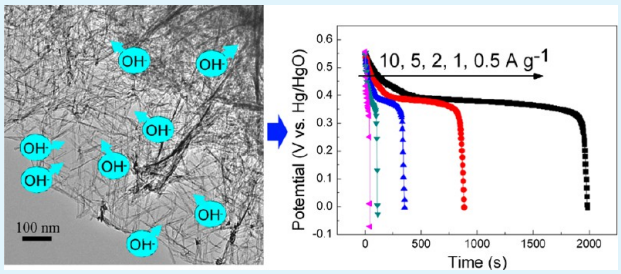

KEYWORDS: *solvothermal, mesoporous microspheres, α-Ni(OH)$_2$, supercapacitor*

1. INTRODUCTION

Compared with other electrochemical energy storage devices, supercapacitor can deliver higher power density. Besides, supercapacitor usually has long and stable cycle life. And it is environmentally friendly.[1−3] So it has been regarded as one of the most promising energy storage devices in practical use. Electrode materials widely used in supercapacitors are carbon, conducting polymers and metal oxides/hydroxides. Supercapacitors using carbon materials are electric double layer capacitors(EDLCs), of which the capacitances are generated from the charge separation at the electrode/electrolyte interface. Currently, most commercial EDLCs use carbonaceous materials with high-surface-areas as electrode materials. No matter the electrolyte is aqueous or organic, the energy density of EDLCs is about 3−6 Wh/kg.[4] Such low energy density is insufficient to meet the increasing demand of high energy and power density in modern devices. Supercapacitors using conducting polymers or metal oxides/hydroxides are pseudocapacitors(PCs). Their capacitances arise from electrochemical adsorption of ions or redox reactions. Faradaic pseudocapacitance usually occurs at or near the electrode surface and the processes are usually fast and reversible.[1] However, most of the oxide materials are not suitable for industrial use because of their high cost.

Recently, Ni(OH)$_2$ has been considered as an attractive candidate in supercapacitor because of its high theoretical specific capacitance and excellent redox behavior. Besides, Ni(OH)$_2$ is environmentally friendly and inexpensive.[5−10] Ni(OH)$_2$ has two phases: α- and β-Ni(OH)$_2$. The β-phase is composed of well-oriented Ni(OH)$_2$ layers. In α-Ni(OH)$_2$, there are many exchangeable anions and water molecules intercalated into the interlayer. So the interlayer space of α-Ni(OH)$_2$ is larger than the β-phase, which endows it better electrochemical activity. In addition, α-Ni(OH)$_2$ transforms to γ-NiOOH after the charging process, in which the oxidation state of Ni is about 3.3 to 3.7.[11] Whereas in β-NiOOH(the charged state of β-Ni(OH)$_2$), the oxidation state of Ni is about 2.9. That is to say, in the electrochemical process, the α-Ni(OH)$_2$/γ-NiOOH pair can deliver more electrons than β-Ni(OH)$_2$/β-NiOOH. So α-Ni(OH)$_2$ usually shows better electrochemical performance than β-Ni(OH)$_2$. However, the α-Ni(OH)$_2$ phase is hard to prepare because it is unstable and can easily transform to β-Ni(OH)$_2$.

Materials with the 3D hierarchical structures can significantly shorten the diffusion lengths for both electrolyte ions and electrons. Considering that most of the reactions of supercapacitors occur at or near the surface of electrodes, materials with high surface area and suitable pore sizes (2−5 nm) usually display higher discharge specific capacitance because it is easily immersed by electrolytes.[12] Besides, the proton transfer of electrolytes within the pores can be eased. As the reaction speed of charge/discharge is rapid in supercapacitors, these structures are favorable for improving the electrochemical utilization of active materials.[13]

In this paper, α-Ni(OH)$_2$ microspheres constructed of nanowires were prepared through a solvothermal method using triethylene glycol(TEG) and water as the mixed solvent. The as-obtained α-Ni(OH)$_2$ microspheres display an ultrahigh

Received: April 12, 2013
Accepted: June 25, 2013
Published: June 25, 2013

surface area of 318 m^2 g^{-1}. This sample shows high specific capacitance and excellent rate performance when used as electrode material of supercapacitors.

2. EXPERIMENTAL SECTION

2.1. Synthesis of Mesoporous $Ni(OH)_2$. Mesoporous $Ni(OH)_2$ were prepared through a simple solvothermal method. All reagents were used as purchased without purification. In a typical procedure, $Ni(NO_3)_2{\cdot}6H_2O$ (1.45 g) was dissolved in the water/polyol mixed solvent. Then urea (0.6 g) was thrown into the solution. After a homogeneous solvent was formed by stirring, the resulting solution was transferred into a Teflon-lined stainless steel autoclave (100 mL in volume) and heated at 120 °C for 24 h. After the autoclave was cooled down to room temperature, the precipitates were collected by filtration, washed with distilled water and absolute ethanol for 3 times, respectively. Finally it was dried at 60 °C for 12 h before characterization.

2.2. Characterization of Mesoporous α-$Ni(OH)_2$. X-ray diffraction patterns were recorded using powder diffraction diffractometer (Rigaku D/max-2500, Cu Kα radiation). Scanning electron microscopy (SEM) images were taken with a JEOL JSM 7500F apparatus. Transmission electron microscopy (TEM) images were obtained on a FEI Tecnal G2F 20 instrument at an acceleration voltage of 200 kV. Fourier transform infrared spectrum(FTIR) was recorded on a Nicolet Magna 560 IR Spectrometer. N_2 adsorption−desorption was tested on Micromeritics Tristar-3000.

2.3. Electrochemical Characterization of Mesoporous α-$Ni(OH)_2$. Battery performance was determined on the LAND CT2001A multichannel galvanostat. The potential range adopted during the charge/discharge process is 0−0.55 V(vs Hg/HgO). And the discharge current densities are 0.5, 1, 2, 5, and 10 A g^{-1}, respectively. Three-electrode system were employed using Hg/HgO electrode as the reference electrode, foam nickel as the counter electrode and mesoporous α-$Ni(OH)_2$ as the active material of working electrode. The weight ratio of active material, acetylene black, and PVDF binder in the working electrode is 80:15:5. The electrolyte was 2 M KOH. Cyclic voltammogram(CV) and the electrochemical impedance spectroscopy(EIS) tests were conducted on a Zahner IM6e electrochemical workstation. CV tests were done between 0 and 0.6 V and the scan rate was 5 mV s^{-1}. EIS was performed in the frequency range of 0.01−100K Hz with an amplitude of 5 mV.

3. RESULTS AND DISCUSSIONS

The panoramic image(Figure 1a) of the sample prepared in TEG/H_2O mixed solvent (TEG/H_2O = 1/1, herein the ratios describing the solvent are all volume ratios) displays an almost uniform sphere-like morphology (4−5 μm in diameter). High-magnification SEM images in Figure 1b and TEM images in Figure 1c and 1d reveal that the network-like hierarchical microspheres are made of ultrathin nanowires with diameters of 3−5 nm. These nanowires are interconnected with each other with random directions. The surfaces of them are rough and porous. Inset in Figure 1d is the corresponding selected area electron diffraction(SAED) pattern of the α-$Ni(OH)_2$ microspheres. The diffuse rings in it indicate that the nanowires, as self-assembly building blocks of the microflower-like α-$Ni(OH)_2$, are polycrystalline. The high-resolution TEM-(HRTEM) image shows that a nanowire consists of many tiny nanocrystals. The lattice spacing of ~2.16 and 1.97 Å corresponds to those of the (015) and(018) planes(Figure 1e). Because of the intercrossing of wires, the microsphere owns abundant defects and pore canals(Figure 1e).

The strongest reflection at 2θ of 12.7° in the XRD pattern of the as-obtained sample(Figure 2a) exhibits typical features of α-

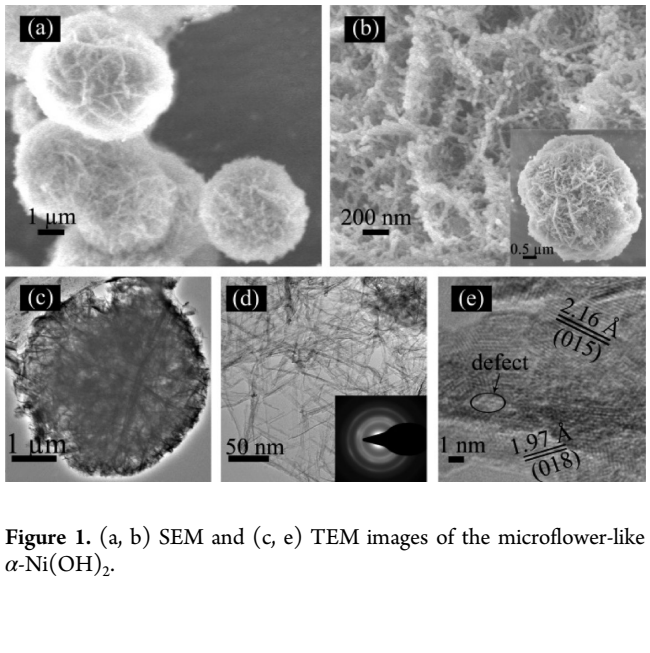

Figure 1. (a, b) SEM and (c, e) TEM images of the microflower-like α-$Ni(OH)_2$.

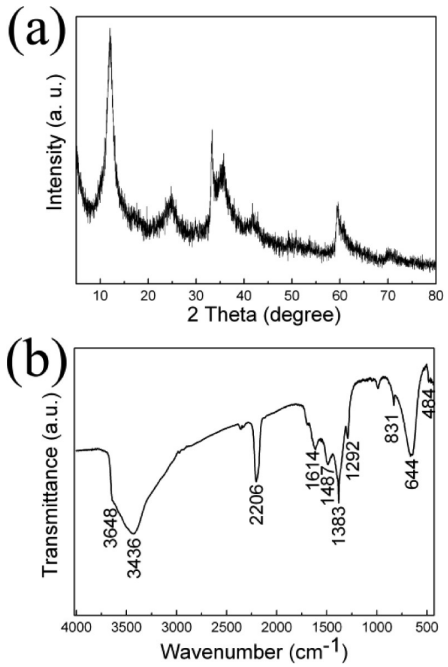

Figure 2. (a) XRD pattern of the microflower-like α-$Ni(OH)_2$ and (b) FTIR spectrum of the microflower-like α-$Ni(OH)_2$.

$Ni(OH)_2$.[14] No other peaks except α-$Ni(OH)_2$ is detected, illustrating its high purity.[15] The peak at 20.5° corresponding to the(002) plane has a slight shift, which can be assigned to the intercalation of some anions(CO_3^{2-}, OCN^- and NO_3^-) into the lattice of the $Ni(OH)_2$ nanocrystals. The degree and type of these anions can cause the interlayer spacing change of α-$Ni(OH)_2$.[15,16] The XRD diffraction peaks of the sample are low and broad, revealing the poor crystallinity and small size of crystallite.

FTIR spectrum in Figure 2b further confirms the composition of α-$Ni(OH)_2$. The vibrational bands at approximately 3648, 3436, 2206, 1614, 1383, 1292, 644, and 484 cm^{-1} are typically detected in α-type hydroxides.[17] The narrow band at ~3648 cm^{-1} is attributed to the ν_{OH} of the free hydroxyl groups in the brucite-like structure.[17,18] A broad band at ~3436 cm^{-1} is the result of the ν_{O-H} vibration of interlayer water molecules and H-bound OH group located in the

turbostratic structure of α-$Ni(OH)_2$. The absorption band at 2206 cm^{-1} stems from the $\nu_{C\equiv N}$ vibration of OCN^- anion.[19] The band at ~1614 cm^{-1} is attributed to the δ_{O-H} vibration of the interlayer water molecules.[20] The absorption at around 1487 cm^{-1} is assigned to the $\nu_{C=O}$ in the carbonate ions.[15] The intercalated OCN^- and carbonate ions are the byproducts of the urea hydrolysis. The vibration bands at 1383, 1292, and 831 cm^{-1} correspond to the vibration of NO_3^-.[15,20,21] The broadening peak at 1383 and 831 cm^{-1} may suggest an interaction of NO_3^- anions with the intercalated water, hydroxyl groups, and nickel cations in the α-$Ni(OH)_2$ layers.[22,23] The band at ca. 644 cm^{-1} is assigned to δ_{O-H} and the band at ~484 cm^{-1} can be attributed to ν_{Ni-OH}.[18,24]

Time dependent experiments were conducted to evoke the formative process of the microflower-like α-$Ni(OH)_2$. SEM images of the sample obtained at different solvothermal times are illustrated in Figure 3. Figure 3a–3f are the enlarged surface

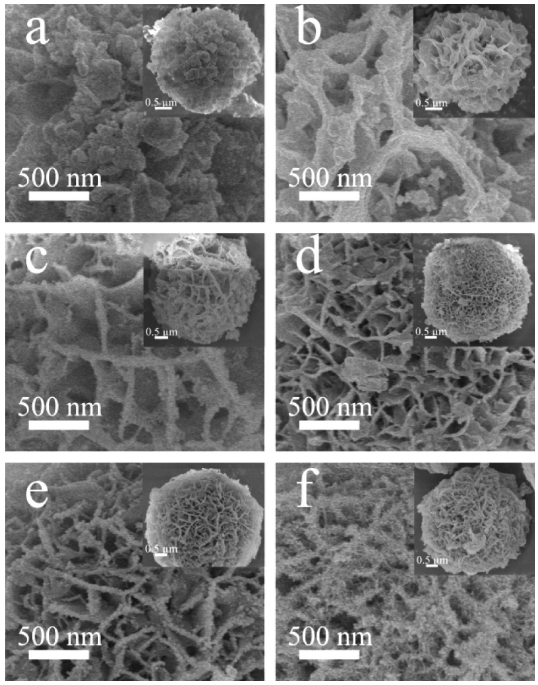

Figure 3. SEM images of α-$Ni(OH)_2$ products obtained at (a) 2, (b) 4, (c) 6, (d) 8, (e) 12, and (f) 16 h.

morphology of α-$Ni(OH)_2$ produced at the corresponding time. Inset pictures show the panoramic morphologies of them. As it can be seen, after a nucleation process for about 2 h, the α-$Ni(OH)_2$ microspheres composed of compact aggregates appear. Then, through dissolution and recrystallization, the compact microspheres are divided into divisive thin sheets. With the prolonging of reaction time, in order to reduce the surface energy, the divisive thin sheets gradually change to net-like hierarchical assemblies, then to microspheres composed of nanowires. Ostwald ripening process may play important roles in this procedure.[15,25,26]

To study the influence of solvents on the morphology of the sample, polyols with different chain lengths and amounts of hydroxyl groups were used as cosolvents with water in the synthetic process. SEM images of them are listed in Figure 4. Those obtained in pure water are also listed in Figure 4d for comparison. As is shown in Figure 4a, sphere-like morphology constructed by nanosheets intersecting with each other is

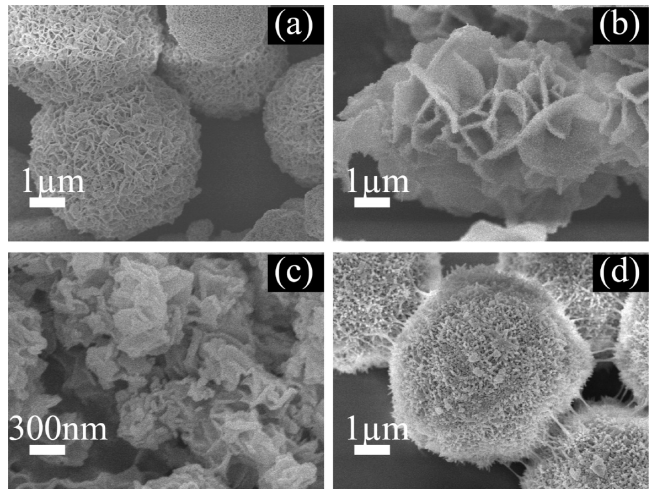

Figure 4. SEM images of the sample prepared in different solvents: (a) $EtOH/H_2O$ = 1/1, (b) EG/H_2O = 1/1, (c) $glycerol/H_2O$ = 1/1, and (d) H_2O.

obtained when $EtOH/H_2O$ is used as the solvent(about 5 μm in diameter). Scattered petals in the micrometer range domain the morphology of the sample with EG/H_2O as the solvent (Figure 4b). There are also many filaments distributing on the petal surface. The size of the particles is obviously decreased when changing the solvent to $glycerol/H_2O$. And the morphology of them tends to be more irregular, which may be ascribed to the high viscosity of glycerol (Figure 4c). It is reported that the dielectric constant of the solvent and the chain length of the alcohols may greatly affect the final morphology of the product.[27] Solvent with a high dielectric constant usually avails the dissociation of ionic bonds and the weakening of electrostatic interactions within crystals. In addition, the polarity of the solvents can affect the dispersity of the reactants in the reaction medium, the nucleus formation of the products, and the preferential growth direction of the growth units. The polarity as well as the dielectric constant of the alcohols used in this work is according to the following order: H_2O > glycerol > TEG > EG > EtOH. Compared with other solvents, TEG has longer chain length, moderate polarity and viscosity. So the products obtained in this TEG/H_2O solvent tend to have kinetically slower growth rate. The as-obtained nanocrystals have time to rotate adequately and find the low-energy configuration interface. Then growth units with oriented growth direction are formed.[28] These building blocks coalesce and aggregate together to form microspheres. To reduce the surface energy of the system, the loose-packed building units of microspheres are divided into nanosheets, then to nanowires.[29] If the viscosity of the solvent is too high (taking glycerol for example), the crystalline growth rate is faster than nucleation rate, resulting in irregular shapes. As the reactants disperse more homogeneously in H_2O than in mixed solvents, the hierarchical structure of the products is not so obvious as others. On the other hand, the polarities of alcohols constructing the solvents are different with water. So these alcohols can serve as surfactant on the surface of the $Ni(OH)_2$ nanoparticles, thus controlling the assembly and growth of them. As the chain length and the number of reactive oxygen are different in different alcohols, they may have different adsorption ability. That is why the size and thickness of building blocks are not the same. And the curvature and aggregation degree of the hierarchical structures are different.[30]

Urea plays an important role in the preparation of α-$Ni(OH)_2$ microspheres. First of all, the hydrolysis of urea slowly produces OH^- in the reaction system because of the reaction shown in eq 1

$$CO(NH_2)_2 + 3H_2O \rightarrow 2NH_4^+ + CO_2 + 2OH^- \quad (1)$$

Considering the mild hydrothermal temperature of 120 °C, we adopted in the reaction, the release rate of OH^- in the system is moderate, which is helpful to control the reaction between nickel ions and OH^- proceeding at a moderate speed, leading to the regular microsphere shape of the final product. Second, for urea hydrolysis, the final pH was around 6.8; which is helpful for the formation of α-$Ni(OH)_2$. However, if the alkalinity of the precipitating agent is too strong, sodium hydroxide or ammonia for example, β-$Ni(OH)_2$ is the preferred product.

In addition, as is shown in Figure 2b, CNO^-, OCN^-, and carbonate ions are produced via the hydrolysis of urea in the starting materials, which can be explained from the reactions shown in eqs 2 and 3.

$$CO_2 + 2OH^- \rightarrow CO_3^{2-} + H_2O \quad (2)$$

$$H_2NCONH_2 \rightleftharpoons NCO^- + NH_4^+ \quad (3)$$

Based on the results of elemental analyses of the sample, the content of elements intercalated in the sample is in the order 2.01% N, 8.83% C, and 2.91% H. The nitrogen content is contributed by the NO_3^- in the starting materials and the hydrolysis product of urea, such as CNO^- and OCN^-. Cyanate in the LDHs is dominantly N-bonded, beneficial for the stability of the structure.[31] These anions, such as NO_3^-, CNO^-, and OCN^-, carbonate ions and nitrate can adsorb in the interlamellar space with water molecules. So the interlayer space of α-$Ni(OH)_2$ is larger than β-$Ni(OH)_2$,[32] leading to better electrochemical performance than the β-phase.

The specific surface areas and porous structure of the as-prepared α-$Ni(OH)_2$ samples were further investigated by nitrogen adsorption/desorption measurements, as indicated in Figure 5. Summary of the data are listed in Table 1. As is shown

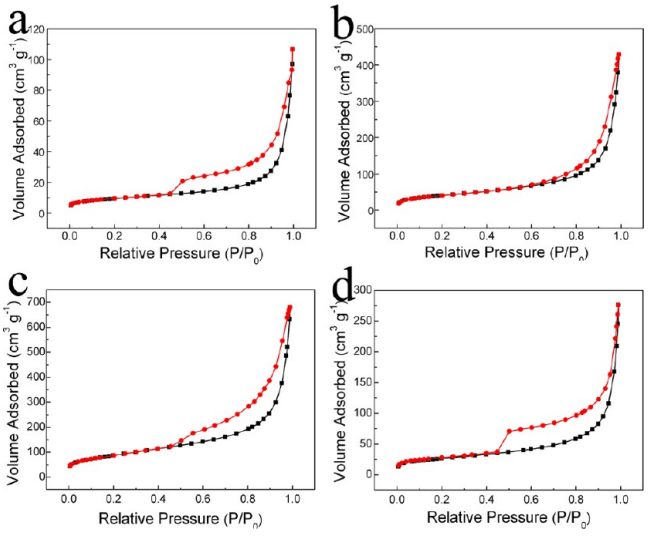

Figure 5. Nitrogen physisorption isotherms of the samples prepared in different solvents: (a) $EtOH/H_2O$ = 1/1, (b) EG/H_2O = 1/1, (c) TEG/H_2O = 1/1, (d) $glycerol/H_2O$ = 1/1.

Table 1. Summary of the BET Surface Areas and Pore Structures of the α-$Ni(OH)_2$ Samples Prepared in Different Solvents

sample	solvent	S_{BET} (m^2 g^{-1})	pore volume (cm^3 g^{-1})	pore diameter (nm)
a	$EtOH/H_2O$ = 1/1	34	0.14	18
b	EG/H_2O = 1/1	149	0.64	5.9
c	TEG/H_2O = 1/1	318	1.02	3.6
d	$glycerol/H_2O$ = 1/1	96	0.41	3.5

in Figure 5, all the four α-$Ni(OH)_2$ samples demonstrate type IV isotherms with H3 hysteresis loops according to Brunauer, Deming, Deming, and Teller(BDDT) classification, which are typical for mesoporous materials.[33] The sample prepared in TEG/H_2O shows a BET surface area of 318 m^2 g^{-1}, which is the highest among the four samples and also higher than the previous data reported for $Ni(OH)_2$.[10,11,26] According to the desorption isotherms by the Barrett–Joyner–Halenda (BJH) method, the sample has a unimodal pore-size distribution with a peak pore size of ~3.6 nm (Figure 6c). Such high surface area

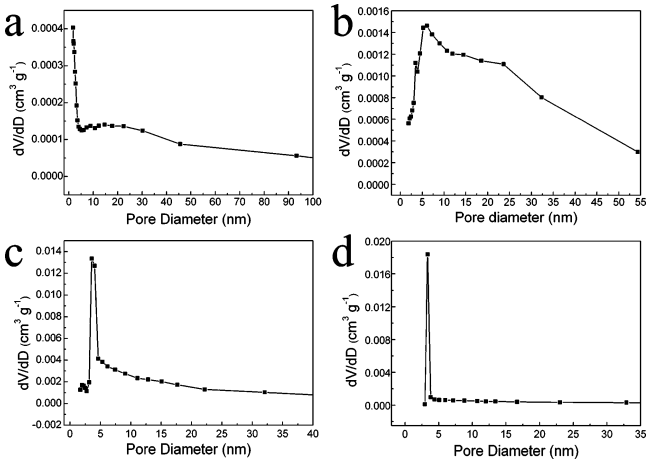

Figure 6. Pore size distribution curves of the samples prepared in different solvents: (a) $EtOH/H_2O$ = 1/1, (b) EG/H_2O = 1/1, (c) TEG/H_2O = 1/1, (d) $glycerol/H_2O$ = 1/1.

and large pore volume of 1.02 cm^3 g^{-1} make its nanometer-sized particles and inner pores easily accessed by electrolytes.[34] Thus the electrode/electrolyte interface is effectively extended. The OH^- transportation through the interface to the electrode during the charge–discharge process is also promoted in supercapacitors.

Galvanostatic charge and discharge measurements were conducted to study the cycle life and rate performance of α-$Ni(OH)_2$. As is shown in Figure 7, After an activation process for about 150 cycles, the sample displays a maximum discharge capacity of 1788.9 F g^{-1} when the discharge current density is set at 0.5 A g^{-1}. This activation process can be assigned to the nature of α-$Ni(OH)_2$. Unlike the β-phase, α-$Ni(OH)_2$ usually needs an activation process to reach the maximum discharge capacity.[35] With cycling, $Ni(OH)_2$ is gradually activated. So the discharge capacitance increases at the initial cycles. On the other hand, the α-$Ni(OH)_2$ microspheres we produced are composed by nanowires. The interconnection between these nanowires may produce many macropores. It takes some time

dx.doi.org/10.1021/am401341h | ACS Appl. Mater. Interfaces 2013, 5, 6643–6648

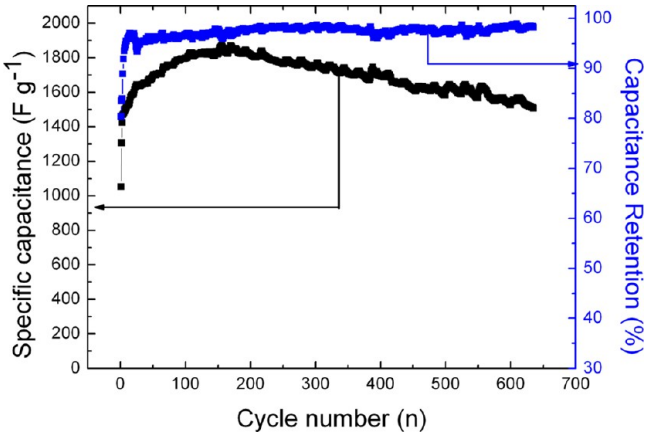

Figure 7. Cyclic performance of α-$Ni(OH)_2$ prepared in the mixed solvent of TEG/H_2O at the current density of 0.5 A g^{-1}.

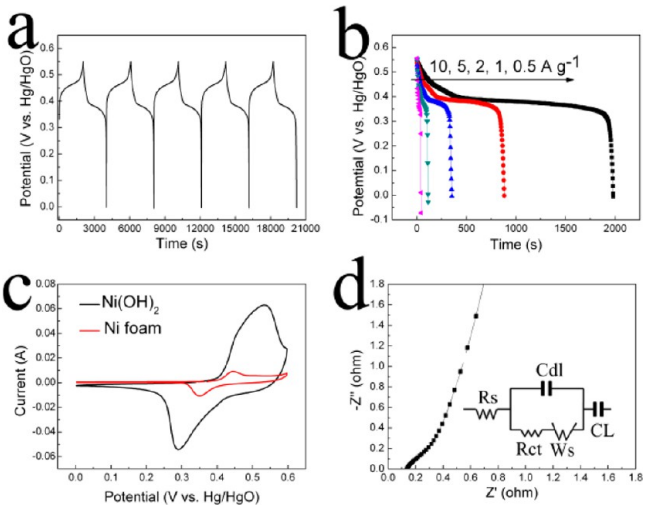

Figure 8. Electrochemical performances of α-$Ni(OH)_2$ prepared in the TEG/H_2O mixed solvent. (a) Typical galvanostatic charge/discharge curve. The measurements were carried out in the 2 M KOH aqueous solution with a constant current of 0.5 A g^{-1}. (b) Galvanostatic discharge curve at various discharge current densities. (c) CV curves of $Ni(OH)_2$ sample and pure Ni foam. (d) Nyquist plot. Inset is the proposed equivalent circuit for the EIS spectrum.

for the electrolyte to immerse the active material sufficiently. And it needs several cycles for the electrode to reach the maximum capacitance.

According to the literature, the theoretical specific capacitance of $Ni(OH)_2$ is 1886.4 F g^{-1} when the voltage window is 0.55 V.[5] The tiny discrepancy between the real specific capacitance and the theoretical one can be attributed to the porous structure of the sample, which is of huge benefit for the effective utilization of $Ni(OH)_2$. As we know, the electrolyte has a penetration depth of approximately 20 nm.[36] Whereas the nanowires constructing the α-$Ni(OH)_2$ microspheres are about 3−5 nm in thickness. They can effectively shorten the proton diffusion distance and make the active materials almost 100% usable for the redox reaction. Furthermore, the interconnection of nanowires creates many larger pores, which is beneficial for electrolyte transport, thus providing a larger surface area for charge transfer reactions. In addition, the BET surface area of the α-$Ni(OH)_2$ microspheres is 318 m^2 g^{-1}. Such large surface area and pore volume are in favor of good penetration of electrolyte into the deep inner region of the electrode, giving rise to sufficient contact between them for energy storage.[37] This hierarchical structure also endows the sample excellent rate performance. As is shown in Figure 8b, the specific capacitance of the sample obtained in TEG/H_2O mixed solvent is 1610.8 F g^{-1} at 1 A g^{-1}, 1296.7 F g^{-1} at 2 A g^{-1}, 1036.2 F g^{-1} at 5 A g^{-1}, and 836.5 F g^{-1} at 10 A g^{-1}, respectively. However, there is inevitable capacitance decay during cycling. After 500 charge−discharge cycles, the specific capacitance is 1527 F g^{-1} at a 0.5 A g^{-1} discharge current density. It is reported that at relatively low discharge current densities, the phase transformation from α-$Ni(OH)_2$ to β-$Ni(OH)_2$ dominantly contributes to the capacitance decay in supercapacitors. Whereas the growth of particles and the increase of crystal size is the major contributor for the capacitance decay at higher discharge current densities.[38]

Figure 8a shows several cycles of charge−discharge curves of the α-$Ni(OH)_2$ electrode performed at a current density of 0.5 A g^{-1}. The similarity in all the profiles illustrates their cycle stability. There are two different ranges in the discharge curves. When the potential is lower than 0.3 V, the discharge curve displays linear dependence between time and potential. This range is assigned to the double-layer capacitance behavior of the electrode, which is caused by the charge separation at the electrode/electrolyte interface. When the potential is at the range of 0.55 to 0.3 V, the discharge curve shows a slope variation between time and potential. This feature is typical for pseudocapacitance behavior, arising from the electrochemical adsorption/desorption or redox reaction occurring at or near the surface of electrode.[39]

The CV curves in Figure 8c indicate that the capacitance of the α-$Ni(OH)_2$ sample mainly arises from the Faradaic pseudocapacitor. There is a pair of redox peaks, indicating that the transfer of electron is reversible.[40] The anodic peak is attributed to the reduction of α-$Ni(OH)_2$ to NiOOH and the cathodic peak is assigned to the reversal transformation from NiOOH to α-$Ni(OH)_2$. Reactions taking place during the process is shown in eq 4:[41,42]

$$\alpha\text{-}Ni(OH)_2 + OH^- \leftrightarrow \gamma\text{-}NiOOH + H_2O + e^- \quad (4)$$

The background signal of the Ni foam is also included in Figure 8c for comparison. It is noted that the capacitance contribution from Ni foam is nearly negligible, illustrating that the specific capacitance of this sample mainly arises from the $Ni(OH)_2$ material.

EIS was performed to investigate the electrochemical conductivity behavior of the as-prepared α-$Ni(OH)_2$ sample using Nyquist plots. As is shown in Figure 8d, there are a semicircle at high-frequency and a line at low-frequency. Inset in Figure 8d is the equivalent circuit for the impedance analysis. Cdl is a double-layer capacitor, CL is the limit pseduocapacitor, and W_S is the Warburg impedance.[43] At very high frequencies, the intercept at real part (Z') represents a combined resistance of intrinsic resistance of active material, ionic resistance of electrolyte, and contact resistance at the active material/current collector interface (Rs).[44] In this experiment, the Rs value is 0.14 Ω, which is lower than most of the literatures, illustrating that excellent contact between electrolyte and active materials is obtained.[45,46] The line in the low frequency is called Warburg resistance (Ws), which is caused by the diffusive resistance of the electrolyte into the pores of the electrode and the proton diffusion in the active materials. A near vertical line at low frequency indicates that the kinetics of ion diffusion in the

dx.doi.org/10.1021/am401341h | ACS Appl. Mater. Interfaces 2013, 5, 6643−6648

solution and the adsorption of ions onto the electrode surface occur swiftly. These findings demonstrate that the electrochemical process on the electrode is not controlled by diffusion. All these features make this α-$Ni(OH)_2$ sample promising as an electrode material of supercapacitor.

4. CONCLUSIONS

Flower-like α-$Ni(OH)_2$ microspheres composed of nanowires are prepared through a solvothermal method using triethylene glycol and water as the solvent. The sample displays an ultrahigh BET surface area of 318 m^2 g^{-1}, beneficial for the sufficient contact between electrolytes and the electrochemical active materials. When used as electrode materials of supercapacitors, the sample shows a high specific capacitance of 1788.9 F g^{-1} at a current density of 0.5 A g^{-1} and excellent rate performance. In view of its easy synthesis, environmental friendliness, and excellent electrochemical performance, this α-$Ni(OH)_2$ sample is promising in electrochemical supercapacitors.

AUTHOR INFORMATION

Corresponding Author

*Fax: 86-022-23502604. Tel: 86-022-23504527. E-mail: jiaolf@nankai.edu.cn.

Notes

The authors declare no competing financial interest.

ACKNOWLEDGMENTS

This work was financially supported by 973 program(2010CB631303), NSFC(21073100, 51231003), TSTC(10JCYBJC08000, 11JCYBJC07200,10SYSYJC27600), and 111 Project(B12015).

REFERENCES

(1) Simon, P.; Gogotsi, Y. *Nat. Mater.* **2008**, *7*, 845−854.
(2) Liu, C.; Li, F.; Ma, L. P.; Cheng, H. M. *Adv. Mater.* **2010**, *22*, E28−E62.
(3) Miller, J. R.; Burke, A. F. *ECS Interface* **2008**, *17*, 53−57.
(4) Long, J. W.; Bélanger, D.; Brousse, T.; Sugimoto, W.; Sassin, M. B.; Crosnier, O. *MRS Bull.* **2011**, *36*, 513−522.
(5) Lu, Z. Y.; Chang, Z.; Zhu, W.; Sun, X. M. *Chem. Commun.* **2011**, *47*, 9651−9653.
(6) Kong, X. H.; Liu, X. B.; He, Y. D.; Zhang, D. S.; Wang, X. F.; Li, Y. D. *Mater. Chem. Phys.* **2007**, *106*, 375−378.
(7) Wang, H. L.; Casalongue, H. S.; Liang, Y. Y.; Dai, H. J. *J. Am. Chem. Soc.* **2010**, *132*, 7472−7477.
(8) Bastakoti, B. P.; Huang, H. S.; Chen, L. C.; Wu, K. C. W.; Yamauchi, Y. *Chem. Commun.* **2012**, *48*, 9150−9152.
(9) Wang, H. L.; Liang, Y. Y.; Mirfakhrai, T.; Chen, Z.; Casalongue, H. S.; Dai, H. J. *Nano Res.* **2011**, *4*, 729−736.
(10) Li, B. J.; Ai, M.; Xu, Z. *Chem. Commun.* **2010**, *46*, 6267−6269.
(11) Tong, G. X.; Liu, F. T.; Wu, W. H.; Shen, J. P.; Hu, X.; Liang, Y. *CrystEngComm* **2012**, *14*, 5963−5973.
(12) Wei, T. Y.; Chen, C. H.; Chien, H. C.; Lu, S. Y.; Hu, C. C. *Adv. Mater.* **2010**, *22*, 347−351.
(13) Yan, J.; Fan, Z. J.; Sun, W.; Ning, G. Q.; Wei, T.; Zhang, Q.; Zhang, R. F.; Zhi, L. J.; Wei, F. *Adv. Funct. Mater.* **2012**, *22*, 2632−2641.
(14) Ren, Y.; Gao, L. *J. Am. Ceram. Soc.* **2010**, *93*, 3560−3564.
(15) Xu, L. P.; Ding, Y. S.; Chen, C. H.; Zhao, L. L.; Rimkus, C.; Joesten, R.; Steven, L. S. *Chem. Mater.* **2008**, *20*, 308−316.
(16) Jiang, H.; Zhao, T.; Li, C. Z.; Ma, J. *J. Mater. Chem.* **2011**, *21*, 3818−3823.
(17) Portemer, F.; Delahaye-Vidal, A.; Figlarz, M. *J. Electrochem. Soc.* **1992**, *139*, 671−678.
(18) Jeevanandam, P.; Koltypin, Y.; Gedanken, A. *Nano Lett.* **2001**, *1*, 263−266.
(19) Mavis, B.; Akinc, M. *Chem. Mater.* **2006**, *18*, 5317−5325.
(20) Taibi, M.; Ammar, S.; Jouini, N.; Fiévet, F.; Molinié, P.; Drillon, M. *J. Mater. Chem.* **2002**, *12*, 3238−3244.
(21) Xu, Z. P.; Zeng, H. C. *Chem. Mater.* **1999**, *11*, 67−74.
(22) Liu, B. H.; Yu, S. H.; Chen, S. F.; Wu, C. Y. *J. Phys. Chem. B* **2006**, *110*, 4039−4046.
(23) Chisem, I. C.; Jones, W. *J. Mater. Chem.* **1994**, *4*, 1737−1744.
(24) Deabate, S.; Fourgeot, F.; Henn, F. *J. Power Sources* **2000**, *87*, 125−136.
(25) Li, X. W.; Xiong, S. L.; Li, J. F.; Bai, J.; Qian, Y. T. *J. Mater. Chem.* **2012**, *22*, 14276−14283.
(26) Luo, Z. J.; Wang, K.; Li, H. M.; Yin, S.; Guan, Q. F.; Wang, L. G. *CrystEngComm* **2011**, *13*, 7108−7113.
(27) Liu, H. B.; Xiang, L.; Jin, Y. *Cryst. Growth Des.* **2006**, *6*, 283−286.
(28) Banfield, J. F.; Welch, S. A.; Zhang, H. Z.; Ebert, T. T.; Penn, R. L. *Science* **2000**, *289*, 751−754.
(29) Zhang, J.; Sun, L. D.; Yin, J. L.; Su, H. L.; Liao, C. S.; Yan, C. H. *Chem. Mater.* **2002**, *14*, 4172−4177.
(30) Wang, L.; Zhao, Y.; Lai, Q. Y.; Hao, Y. J. *J. Alloys Compd.* **2010**, *495*, 82−87.
(31) Soler-Illia, G. J. d. A. A.; Jobbágy, M.; Regazzoni, A. E.; Blesa, M. A. *Chem. Mater.* **1999**, *11*, 3140−3146.
(32) Delahaye-Vidal, A.; Beaudoin, B.; Sac-Epée, N.; Tekaia-Elhsissen, K.; Audemer, A.; Figlarz, M. *Solid State Ionics* **1996**, *84*, 239−248.
(33) Sing, K. S. W.; Everett, D. H.; Haul, R. A. W.; Moscou, L.; Pierotti, R. A.; Rouquérol, J.; Siemieniewska, T. *Pure Appl. Chem.* **1985**, *57*, 603−619.
(34) Zhou, J. B.; Tang, C.; Cheng, B.; Yu, J. G.; Jaroniec, M. *ACS Appl. Mater. Interfaces* **2012**, *4*, 2174−2179.
(35) Mavis, B.; Akinc, M. *J. Power Sources* **2004**, *134*, 308−317.
(36) Hu, C. C.; Chang, K. H.; Lin, M. C.; Wu, Y. T. *Nano Lett.* **2006**, *6*, 2690−2695.
(37) Guo, Y. G.; Hu, J. S.; Wan, L. J. *Adv. Mater.* **2008**, *20*, 2878−2887.
(38) Hu, G. X.; Li, C. X.; Gong, H. *J. Power Sources* **2010**, *195*, 6977−6981.
(39) Sugimoto, W.; Iwata, H.; Yasunaga, Y.; Murakami, Y.; Takasu, Y. *Angew. Chem., Int. Ed.* **2003**, *42*, 4092−4096.
(40) Liang, Y. Y.; Bao, S. J.; Li, H. L. *J. Solid State Electrochem.* **2006**, *11*, 571−576.
(41) Xu, M. W.; Bao, S. J.; Li, H. L. *J. Solid State Electrochem.* **2006**, *11*, 372−377.
(42) Liu, Z. L.; Tay, S. W.; Li, X. *Chem. Commun.* **2011**, *47*, 12473−12475.
(43) Stoller, M. D.; Park, S.; Zhu, Y. W.; An, J.; S., R. R. *Nano Lett.* **2008**, *8*, 3498−3502.
(44) Gamby, J.; Taberna, P. L.; Simon, P.; Fauvarque, J. F.; Chesneau, M. *J. Power Sources* **2001**, *101*, 109−116.
(45) Zhu, J. W.; Chen, S.; Zhou, H.; Wang, X. *Nano Res.* **2011**, *5*, 11−19.
(46) Chen, S.; Zhu, J. W.; Zhou, H.; Wang, X. *RSC Adv.* **2011**, *1*, 484−489.